One Nanometer HfO_2-Based Ferroelectric Tunnel Junctions on Silicon

Suraj S. Cheema, Nirmaan Shanker, Cheng-Hsiang Hsu, Adhiraj Datar, Jongho Bae, Daewoong Kwon, and Sayeef Salahuddin**

ABSTRACT: In ferroelectric materials, spontaneous symmetry breaking leads to a switch-able electric polarization, which offers significant promise for nonvolatile memories. In particular, ferroelectric tunnel junctions (FTJs) have emerged as a new resistive switching memory which exploits polarization-dependent tunnel current across a thin ferroelectric barrier. This work integrates FTJs with com-plementary metal-oxide-semiconductor-compatible Zr-doped HfO_2 (Zr:HfO_2) ferroelectric barriers of just 1 nm thickness, grown by atomic layer deposition on silicon. These 1 nm Zr:HfO_2 tunnel junctions exhibit large polarization-driven electroresistance (>20 000%), the largest value reported for HfO_2-based FTJs. In addition, due to just a 1 nm ferroelectric barrier, these junctions provide large tunneling current (>1 A cm^{-2}) at low read voltage, orders of magnitude larger than reported thicker HfO_2-based FTJs. Therefore, this proof-of-principle demonstration provides an approach to simultaneously overcome three major drawbacks of prototypical FTJs: a Si-compatible ultrathin ferroelec-tric, large electroresistance, and large read current for high-speed operation.

1. Introduction

Ferroelectric materials are of great technological interest for nonvolatile memories[1,2] due to collectively-ordered electrical dipoles whose polarization can be switched under an applied voltage.[3] Most ferroelectric research has traditionally focused on perovskite-structure oxides.[4] Perovskites, however, suffer from various chemical, thermal, lattice, and interfacial oxide incompatibilities with silicon and modern semiconductor processes.[5] Since the discovery of ferroelectricity in HfO_2-based thin films in 2011,[6] fluorite-structure binary oxides have attracted considerable interest as they are compatible with complementary metal-oxide-semiconductor (CMOS) processes.[7] Accordingly, HfO_2-based ferroelectric memory has received significant attention in recent years,[1,8,9] primarily focused on charge-based ferroelectric random access memory (FeRAM) and ferroelectric field effect transistors (FeFETs).[2,10] Meanwhile, resistive-switching materials—which exhibit electrically-induced resistance changes in metal-dielectric-metal junctions or heterostructures with multi-dielectric barriers—have emerged as promising candidates for novel beyond-CMOS data-centric computing paradigms.[11–13] In this context, ferroelectric tunnel junctions (FTJs) present a promising energy-efficient resistive switching memory[12,13] as FTJs exploit the ferroic polarization functionality of the insulating barrier.[14] Voltage-controlled polarization-dependent tunneling through the ferroelectric layer (tunnel electroresistance, TER) can yield much larger ON/OFF conductance ratios[15,16] than, for example, current-controlled magnetic tunnel junctions,[12] another two-terminal tunneling resistive switching device.

A critical requirement for FTJs is to achieve a sufficiently high tunneling current (J_{ON}) at the ON state to ensure that a scaled device can be read rapidly, while still exhibiting a large TER ((J_{ON}-J_{OFF})/J_{OFF} × 100%).[13] Considering the large band gap of HfO_2 (≈6 eV), the thickness of HfO_2 in the FTJ will need to be reduced to the ultrathin limit for adequate tunnel current. Tunnel junctions implementing CMOS-compatible HfO_2-based ferroelectric barriers have been recently demonstrated,[17–19] but even three nanometer Zr-doped HfO_2 (Zr:HfO_2) barriers were found to be too thick to obtain nano-ampere level current in micron-sized capacitors.[20] Therefore, high ON current is a critical consideration; however, the increased ON state current from an ultrathin barrier will coincide with an increased OFF state current. For array-level implementations, where sneak leakage paths can lead to increased power consumption, selector devices may be required in conjunction with the FTJ memory elements to reduce such sneak currents.[13] Here, we demonstrate FTJs utilizing one nanometer Zr:HfO_2 as the ferroelectric barrier, grown by atomic layer deposition (ALD) directly on silicon, thereby scaling down the tunnel barrier

S. S. Cheema
Department of Materials Science and Engineering
University of California
Berkeley, CA 94720, USA
E-mail: s.cheema@berkeley.edu
N. Shanker, C.-H. Hsu, A. Datar, J. Bae, D. Kwon,[+] S. Salahuddin
Department of Electrical Engineering and Computer Sciences
University of California
Berkeley, CA 94720, USA
E-mail: sayeef@berkeley.edu
S. Salahuddin
Materials Sciences Division
Lawrence Berkeley National Laboratory
Berkeley, CA 94720, USA

thickness almost to the nanoscale limit. Robust ferroelectricity in ultrathin Zr:HfO_2 films was recently theoretically[21,22] and experimentally[23,24] established. Notably, opposing conventional scaling trends observed in perovskite ferroelectrics,[25] ferroelectricity is enhanced rather than suppressed with decreasing thickness in Zr:HfO_2 films down to 1 nm thickness.[23] Accordingly, FTJs integrating these 1 nm Zr:HfO_2 tunnel junctions exhibit large polarization-driven TER (>20,000%), the largest reported for HfO_2-based FTJs. In addition, these FTJs demonstrate large tunnel current (J_{ON} > 1 A cm^{-2} at low read voltage), orders of magnitude larger than reported thicker HfO_2-based FTJs.[18,19] The robust FTJ operation with the ferroelectric barrier scaled down almost to the physical limit on Si, and the simultaneous occurrence of large TER with large tunnel current, highlight the potential of HfO_2-based FTJs for ultra-scaled memory applications.

2. Results and Discussion

2.1. Polarization-Driven Switching in 1 nm HfO_2-Based FTJs

One nanometer films of Zr:HfO_2 are grown by 10 cycles of ALD (4:1 Hf:Zr cycle ratio) on highly doped silicon wafers (10^{19} cm^{-3}), buffered with approximately one nanometer chemically-grown SiO_2, and capped with 50 nm W metal (Experimental Section). For reference, 10 ALD cycles correspond to approximately 10 Å thickness, as confirmed by synchrotron X-ray reflectivity (XRR, Figure S1, Supporting Information). The ALD growth technique facilitates atomic-level thickness control and conformal deposition for highly scaled semiconductor applications.[26] Post-deposition annealing at 500 °C with W capping is required to stabilize the ferroelectric orthorhombic phase ($Pca2_1$) in doped-HfO_2 via confinement strain[23] rather than the other nonpolar fluorite-structure polymorphs.[8]

Synchrotron X-ray characterization of these bare 1 nm Zr:HfO_2 films (**Figure 1**a) confirms the presence of the polar orthorhombic structure and highly-oriented films via in-plane grazing incidence diffraction (GID, Figure 1b) and 2D reciprocal space maps (Figure 1c), respectively. Specifically, the in-plane geometry allows for sampling of multiple lattice planes and finer-width reflections to enable clear indexing to the polar orthorhombic ($Pca2_1$) fluorite structure in 1 nm Zr:HfO_2 films (Figure 1b). The presence of many reflections, in particular the $Pca2_1$ (110) reflection, from the in-plane GID spectra allow for clear distinction from other nonpolar fluorite-structure polymorphs.[8] Such diffraction spectra would be otherwise prohibited in typical out-of-plane geometry due to the lack of

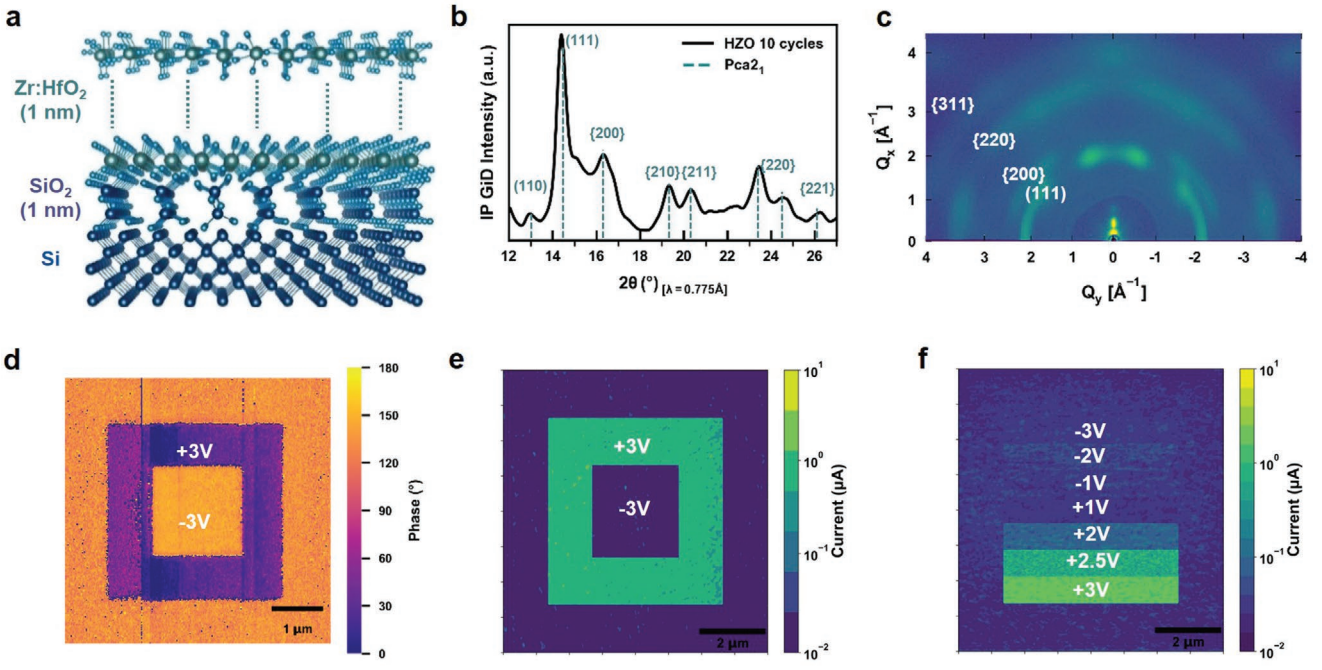

Figure 1. Structural and scanning probe characterization of 1 nm ferroelectric Zr:HfO_2 on Si. a) Schematic of Si/SiO_2/Zr:HfO_2 FTJ heterostructure used for synchrotron XRD and scanning microscopy measurements. Green, blue and light blue atoms correspond to Hf (Zr), Si, and O, respectively. For scanning probe measurements, the highly-doped silicon substrate is grounded and the voltage is applied to the film surface. b) Synchrotron grazing incidence diffraction (GID) measured with in-plane geometry of 1 nm Zr:HfO_2. The in-plane GID pattern indexes to the polar orthorhombic ($Pca2_1$) phase associated with fluorite-structure ferroelectricity. In particular, the (110) reflection rules out the nonpolar tetragonal ($P4_2$/nmc) phase: this reflection is forbidden by the higher tetragonal symmetry. And the position of the (111) reflection and lack of split-peaks rules out the bulk-stable nonpolar monoclinic ($P2_1$/c) phase. c) Synchrotron 2D diffraction in $Q_x - Q_y$ space of 1 nm Zr:HfO_2. The presence of concentrated intensity regions in this reciprocal space slice indicates the highly-textured nature of the ultrathin Zr:HfO_2 film. d,e) Corresponding PFM phase (d) and CAFM current (e) maps measured in the same region of the film after a ± 3V box-in-box voltage profile was applied to the film's surface. Both images show correspondence and support polarization-driven resistive switching. The current map was measured at a fixed DC voltage of 800 mV, well below the coercive voltage. f) CAFM current map after poling the surface with increasing voltages from −3 to +3 V. The onset of the high current state only appears at 2.5 V, consistent with pulsed I–V_{write} hysteresis loops in Figure 2d.

vertical diffraction planes and the large line width inherent to nanometer-thick films.

To examine the link between polarization and tunnel current in 1 nm Zr:HfO_2 bare films, scanning probe microscopy was employed. Piezoresponse force microscopy (PFM) phase maps (Figure 1d) show well-defined regions of 180° phase contrast, corresponding to the two remnant ferroelectric polarization states. In tandem, conductive atomic force microscopy (CAFM) current maps (Figure 1e) on the same poled regions mimic the PFM contrast, consistent with polarization-dependent tunnel current.[27,28] Subsequent CAFM studies poled the Zr:HfO_2 surface with increasing voltage from −3 V (OFF state) to +3 V (ON state). The sharp increase in tunnel current at +2.5 V (Figure 1f) corresponds to the coercive voltage determined from hysteresis measurements (**Figure 2**c,d), providing support toward polarization-driven resistive switching.

To establish polarization switching in 1 nm Zr:HfO_2-based capacitors (Figure 2a), PFM switching spectroscopy demonstrates the presence of 180° phase hysteresis (Figure 2c), consistent with ferroelectricity. More detailed advanced scanning probe characterization which eliminate common electrostatic and electromechanical artifacts have demonstrated ferroelectricity in these 1 nm Zr:HfO_2 films.[23] Pulsed current-voltage (I–V_{write}) measurements (Figure 2d)—applying the same waveform structure as PFM spectroscopy—demonstrate saturating, abrupt hysteretic behavior, with consistent coercive (switching) voltage as the PFM phase loops, again characteristic of polarization-driven switching.[29] Notably, the presence of closed hysteresis likely precludes ionic-driven mechanisms, which have been reported to result in open I–V_{write} loops in HfO_2-based junctions,[30] potentially due to irreversible oxygen vacancy migration. The lack of a forming step at high voltage required to observe resistive hysteretic switching also renders ionic-driven filamentary mechanisms unlikely.

It is worth noting that oxygen-vacancy-based contributions can be intertwined with polarization switching in HfO_2-based systems,[30–34] as recent analytical models have shown that ferroelectric-like behavior in fluorite-based thin films may have electrochemical origins.[35] For example, in the nonpolar fluorite-structure Gd:CeO_2, giant electrostriction has been observed due to oxygen vacancies.[36] Additionally, electrochemical effects have been shown to mimic polarization-like resistive switching[37] as recently demonstrated in perovskite-based tunnel junctions.[37] Furthermore, the possibility of W oxidation under an applied electric field is possible, as the interfacial chemistry of W electrodes and crystalline ferroelectric HfO_2-based films is not yet well-understood.[38] Therefore, to examine potentially confounding ionic and electrochemical contributions in the 1 nm Zr:HfO_2 FTJs, further I–V measurements were performed. In particular, voltage polarity-dependent pulsed I–V measurements (Figure 2d) demonstrate a resistive hysteresis sense independent of the sweep direction, inconsistent with filament formation in electrochemical resistive switching, and consistent polarization-driven resistive switching (Supporting Information). The observed counterclockwise I–V_{write} hysteresis sense can be explained by polarization-induced barrier height modulation in the metal-ferroelectric-insulator-semiconductor (MFIS) structure (Figure 2e). Indeed, linear I–V_{read} measurements fit well to a model considering direct tunneling through a polarization-dependent trapezoidal potential barrier (Figure S2, Supporting Information). Device area-independence of J_{ON} (Figure S3, Supporting Information) further eliminates filamentary-type mechanisms; in filamentary-based resistive switching, the current (density) is expected to be independent (dependent) of device area since the filament provides the majority of the current.[18] Therefore, although the co-existing, and often synergistic[30,34,35] influence of various electrochemical and ionic phenomena intertwined with polarization switching cannot be completely eliminated, multiple I–V signatures in these 1 nm Zr:HfO_2 FTJs indicate minimal contributions from various ionic-driven mechanisms commonly attributed to amorphous hafnia[13] and indicate the observed resistive switching behavior is consistent with ferroelectric polarization switching.

2.2. Device Performance of 1 nm HfO_2-Based FTJs

Regarding device performance in the 1 nm Zr:HfO_2 FTJs, polarization-dependent I–V measurements demonstrate ON/OFF conductance ratios approaching 200 from linear I–V_{read} (**Figure 3**a–c) and 100 from pulsed I–V_{write} hysteresis (Figure 3d), surpassing the previous high-mark around 50[39] observed for HfO_2-based FTJs (**Figure 4**a). Achieving two orders of magnitude ON/OFF conductance ratio not only surpasses all HfO_2-based FTJ literature, but also matches epitaxial perovskite-based FTJs grown by pulsed laser deposition (PLD) on silicon (Figure 4b). Notably, J_{ON}, ≈ 100 nA μm^{-2} measured at low read voltage (Figure 3a,b), is orders of magnitude larger than observed in reported HfO_2-based FTJs employing thicker ferroelectric barriers.[18,19] The read voltage used in all I–V measurements (< 500 mV) is well below the coercive voltage of 1 nm Zr:HfO_2, enabling non-destructive readout. The low J_{ON} (< 10 nA μm^{-2}) reported for HfO_2-based FTJs—due to the lack of an ultrathin Zr:HfO_2 ferroelectric layer only recently established[20–24,40]—prevents practical application into highly-scaled crossbar memories due to insufficient read current.[13]

Here, the 1 nm Zr:HfO_2 FTJs can maintain an ON/OFF of 10—higher than most HfO_2-based FTJs reported thus far (Figure 4a)—for up to 10^3 cycles (Figure 3e). Endurance cycling operates below the optimal switching voltage (+2.8 V, −2.5 V) to prevent dielectric interlayer (SiO_2) breakdown (Figure S4, Supporting Information), a common failure mechanism in HfO_2-based FeFETs.[10] The large TER window in these 1 nm Zr:HfO_2 FTJs affords operation at a lower voltage to enhance endurance at the slight expense of TER. The endurance measurements also provide insights into the potential intertwined role of oxygen vacancies and polarization switching in HfO_2-based ferroelectrics.[34] In particular, wake-up effects in HfO_2-based ferroelectrics have been often attributed to redistribution of oxygen vacancies with field cycling,[41,42] in which current density is expected to increase upon cycling.[42,43] Here, the OFF-state current density stays relatively constant with field cycling, while the ON-state current density decreases with field cycling (Figure 3e). This behavior is in contrast to the aforementioned behavior attributed to oxygen vacancy redistribution; instead, this behavior could be explained by sub-cycling, in which cycling (+2.8/−2.5 V) below the fully-switched coercive voltage

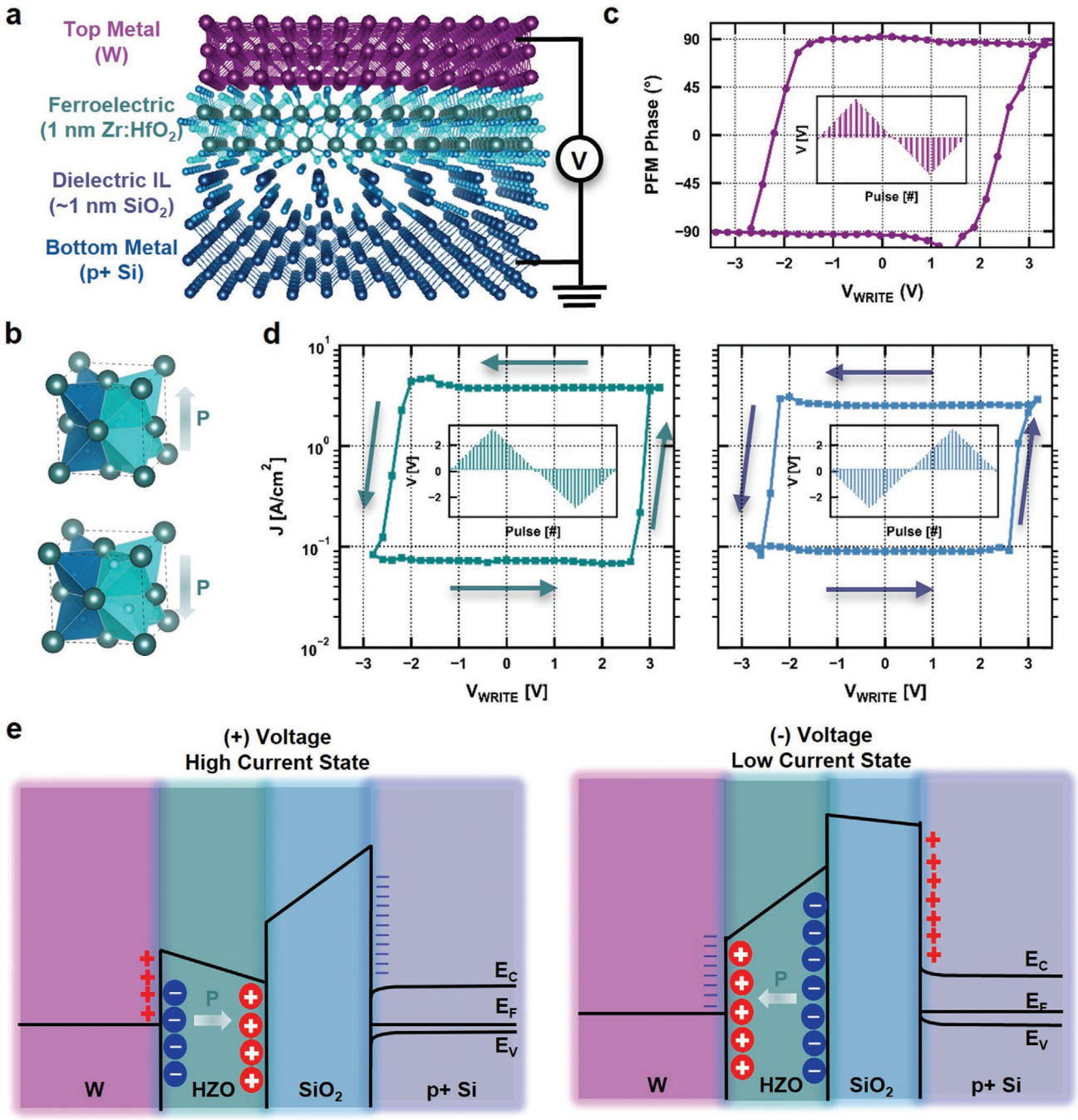

Figure 2. Polarization-driven resistive switching in 1 nm Zr:HfO_2 ferroelectric tunnel junctions. a) Schematic of the Si/SiO_2/Zr:HfO_2/W FTJ heterostructure investigated in this work, utilizing composite tunnel barriers comprised of 1 nm crystalline ferroelectric Zr:HfO_2 and approximately 1 nm amorphous dielectric SiO_2. For electrical measurements, the highly-doped silicon substrate is grounded, and the gate voltage is applied to the W capacitor. b) Crystal structure schematics of the polar orthorhombic fluorite-structure ferroelectric phase ($Pca2_1$), illustrating the two polarization states which dictate the resistive state in the FTJs. The different colored oxygen atoms represent the acentric oxygen atoms (cyan) and the centrosymmetric oxygen atoms (blue) within the surrounding cation (teal) tetrahedron. c) Piezoresponse (phase) switching spectroscopy PFM loop for 1 nm Zr:HfO_2, demonstrating ferroelectric-like hysteresis. More extensive scanning probe microscopy conclusively demonstrating ferroelectricity in these 1 nm Zr:HfO_2 films is reported in a previous work.[23] Inset: Voltage waveform used in PFM switching spectroscopy. d) Pulsed current-voltage (I–V_{write}) hysteresis map as a function of write voltage measured at 200 mV read voltage. The abrupt hysteretic behaviour and saturating tunnelling electroresistance is characteristic of polarization-driven switching, as opposed to filamentary-based switching caused by electrochemical migration (Supporting Information). The device demonstrates voltage polarity-independent current-voltage hysteresis sense: both negative-positive-negative voltage polarity (left) and positive-negative-positive voltage polarity (right) demonstrate counter-clockwise hysteresis. The voltage polarity-dependent I–V hysteresis measurements further rule out filamentary-based resistive switching mechanisms and is consistent with polarization-driven switching (Supporting

(≈ ±3.0 V) has been shown to accelerate remnant polarization decay,[44] which would degrade the TER.

This proof-of-principle 1 nm Zr:HfO_2 FTJ should motivate further work to optimize this trade-off between TER and endurance, perhaps by employing a higher-κ dielectric interlayer to improve the field distribution through the ferroelectric and reduce the field across the dielectric interlayer to prevent dielectric breakdown. Elimination of the dielectric interlayer, for example, depositing Zr:HfO_2 on Ge substrates without a native oxide layer, could enhance the endurance,[45] but would likely diminish the TER without the asymmetry provided by the composite barrier[46] (Figure 4a). Retention measurements demonstrate the large ON/OFF window exceeding 100 can be maintained for at least 10^4 s (Figure 3f), consistent with typical FTJ-based memory reports[9] and less than the intrinsic piezoresponse retention reported in these 1 nm Zr:HfO_2 films.[23] Moreover, tunnel *I–V* measurements across multiple FTJ devices demonstrate consistent TER behavior (Figure 3i): the ON/OFF ratio exceeds 100× for 20 devices (average of 180×).

2.3. Origins of High Tunnel Electroresistance in 1 nm HfO_2-Based FTJs

Beyond the ferroelectric barrier, there are various physical mechanisms within the metal-ferroelectric-insulator-semiconductor (MFIS) structure that could potentially explain the large polarization-driven TER in this 1 nm HfO_2-based FTJ (Supporting Information). For one, MFS structures employing doped semiconductor electrodes enable barrier width modulation via the ferroelectric field effect at the dielectric-semiconductor interface. Accordingly, MFS structures have demonstrated enhanced performance in perovskite-based FTJs,[16] and even HfO_2-based FTJs on Ge[45] (Figure 4a). However, barrier width modulation from the ferroelectric field-effect is not expected to be a major contributor to the observed behavior in this work. The presence of the dielectric SiO_2 interlayer and the high silicon electrode doping level (10^{19} cm^{-3}) is expected to partially screen the Zr:HfO_2 polarization from the silicon interface and result in a negligible depletion region, respectively. The dual ferroelectric-dielectric barrier present in the heterostructure is another candidate mechanism[47]; recent modeling of composite barrier HfO_2-based FTJs predict depolarization fields from the dielectric interlayer to enhance the tunneling asymmetry, and therefore the TER.[48] Another HfO_2-based FTJ model,[46] which combines both of the aforementioned layering effects present in our FTJ structure, found MFIS to be superior to MFIM structures due to the large asymmetry in dielectric screening between the top and bottom electrodes, which can reduce the OFF state current without diminishing the ON state current. This diminished OFF current operation is particularly promising for potential selector-less implementation of FTJ arrays.[13] Therefore, future HfO_2-based experimental studies should further optimize composite ferroelectric-dielectric bilayers[18,19,49,50] for FTJ performance while remaining in the ultrathin regime to maintain sufficient ON current, while also exploring device geometries to reduce standby current for array-level considerations.

Besides electrostatic effects related to the heterostructure stacking, the nature of the ultrathin ferroelectric layer itself can also contribute to the enhanced polarization-driven TER.[16] Perovskite-based FTJs have typically shown larger TER[15,16] than reported HfO_2-based FTJs,[9] potentially due to the enhanced ferroelectric film quality and crystallinity in high-temperature PLD-grown perovskite ferroelectric films on lattice-matched substrates[27] compared to low-temperature ALD-grown polycrystalline films on Si. In fact, ALD-grown Zr:HfO_2 on Ge demonstrates larger TER compared to ALD-grown Zr:HfO_2 on Si,[45] attributed to the enhanced Zr:HfO_2 ferroelectric orthorhombic phase fraction and film quality on Ge.[45] A similar effect can be expected in these ultrathin Zr:HfO_2 films considering they are highly-oriented[23,24] (Figure 1c), in contrast to thicker polycrystalline films.[8] Furthermore, these 1 nm Zr:HfO_2 films display structural signatures of enhanced ferroelectricity[23]; the amplified polar distortions (structural gauges of polarization) in 1 nm films can increase TER considering the barrier height modulation is proportional to polarization.[51] The common trend of diminished polarization as thickness is diminished—often observed in perovskite ferroelectrics[25]—does not hold for ultrathin Zr:HfO_2 films which demonstrate unconventional size effects.[21–24] Therefore, the unique ferroelectric properties of ultrathin Zr:HfO_2[21–24] can help overcome the trade-off between high electroresistance—typically diminishes with decreasing thickness[16,27] —and tunnel current—increases with decreasing thickness—which have previously plagued FTJs.[16] Accordingly, the TER observed in these 1 nm fluorite-structure FTJs exceeds the original landmark 1 nm perovskite-based FTJs[27] and even matches thicker epitaxial perovskite-based FTJs grown on silicon[52,53] (Figure 4b).

3. Conclusion

In summary, we have demonstrated FTJs on silicon in which the Zr:HfO_2 ferroelectric thickness has been scaled down to 1 nm, equivalent to just two fluorite-structure unit cells. These FTJs simultaneously achieve both large TER and ON current, a combination that has eluded HfO_2-based FTJs thus far, and

Information). Inset: Voltage waveform used in the pulsed $I–V_{write}$ measurements; the alternating sequence—staircase write, fixed read—mimics the PFM waveform. e) Electronic band diagrams of the MFIS FTJ corresponding to the high-current (left) and low-current (right) states, depending on polarization direction. The high-current state (positive voltage applied to the W, Zr:HfO_2 polarization points away from W) corresponds to a lower average tunneling barrier, and vice-versa for the low-current state. The uncircled "+" and "–" symbols in the metal and semiconductor represent holes and electrons, respectively, while the circled "+" and "–" symbols in the ferroelectric layer represent the dipole charges in the ferroelectric. In the band diagrams it is assumed that the ferroelectric bound charges at the metal/ferroelectric interface are perfectly screened and therefore the barrier height at the metal/ferroelectric interface is fixed and independent of polarization direction. The barrier width modulation field-effect from the presence of a semiconductor bottom electrode is expected to be negligible (Supporting Information), based on the presence of the dielectric SiO_2 interlayer screening the Zr:HfO_2 polarization, and the the heavy doping (10^{19} cm^{-3}) of the Si (negligible depletion region). Therefore, only the difference in average potential barrier height is considered for determining the high- and low-current states.

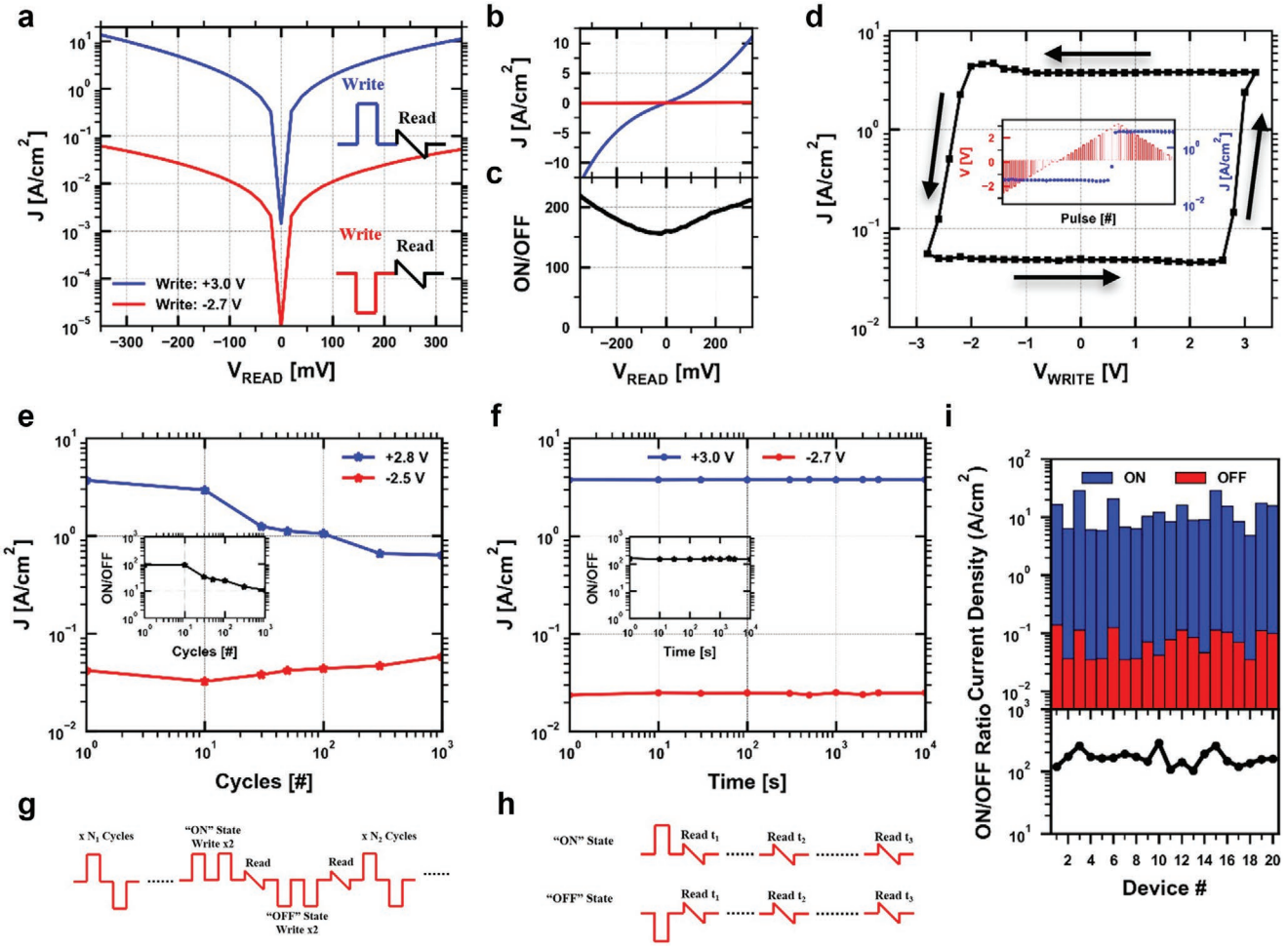

Figure 3. Tunnel electroresistance and device performance in 1 nm Zr:HfO_2 ferroelectric tunnel junctions. a) Linear I–V_{read} measurements after the indicated write voltage (+3.0 V, −2.7 V) was applied to set the Zr:HfO_2 polarization (FTJ current) into its respective state. The I–V_{read} data is consistent with a direct tunneling model considering polarization-dependent tunneling through a trapezoidal barrier (Figure S2, Supporting Information). Inset: Schematic of voltage waveform used to write and read the FTJ current states. b) Tunnel current as a function of read voltage in linear scale to highlight the non-linear I–V_{read} behavior. c) Tunnel electroresistance (TER) ratio as a function of read voltage, demonstrating the maximum ON/OFF conductance ratio exceeding 200 at low read voltage. d) Pulsed I–V_{write} hysteresis map of the read current (measured at 200 mV) as a function of write voltage (up to ± 3 V), demonstrating saturating ON/OFF conductance ratio around 100. Inset: Raw I–V measurement as a function of pulse number to highlight the two stable current states in the FTJ corresponding to the two polarization states in the 1 nm Zr:HfO_2 ferroelectric layer. e) Read current (measured at 200 mV) as a function of endurance cycling (+2.8/−2.5 V write voltages) of the 1 nm Zr:HfO_2 FTJ. Inset: ON/OFF ratio as a function of write cycles, which indicates 10× ON/OFF conductance ratio is maintained up to 10^3 cycles. The endurance of such a thin ferroelectric layer—considering the extensive voltage drop through the amorphous dielectric interlayer (Supporting Information)—is enhanced by operating the FTJ at lower voltage, made possible by the large TER window. f) Read current (measured at 200 mV) as a function of time after the FTJ is set into its respective state by the indicated write voltage (+3.0 V, -2.7 V). These retention measurements indicate the large TER can be maintained for up to 10^4 s, consistent with the lack of decay in previously-reported 1 nm Zr:HfO_2 PFM retention measurements.[23] g,h) Voltage waveform sequence detailing read and write steps for the endurance (c) and retention (d) measurements. i) Read current (measured at 500 mV) and the corresponding ON/OFF ratio after the FTJ is set into its respective state (+3.0 V, −2.7 V) across 20 devices. The ON/OFF ratio across all devices were > 100× (≈ 200×), with an average ON/OFF of 180×.

even competitive with perovskite-based FTJs deposited on Si (Figure 4b).The ability to scale the ferroelectric thickness in an FTJ down to almost the physical thickness limit on silicon and maintain polarization-driven resistive switching offers great potential for high-density memory technology.

4. Experimental Section

Film Deposition: Thin films of Zr:HfO_2 were grown by atomic layer deposition (ALD) in a Fiji Ultratech/Cambridge Nanotech tool at 250 °C in which tetrakis (ethylmethylamino) hafnium and tetrakis (ethylmethylamino) zirconium precursors are heated to 75 °C and water vapor is used as the oxidant. For MFIS capacitor structures, 1 nm chemically-grown SiO_2 on Si was prepared by the standard clean (SC-1) solution (5:1:1 H_2O:H_2O_2:NH_4OH at 80 °C for 10 min) after the Si wafer was cleaned in Piranha (120 °C for 10 min) to remove organics and HF (50:1 H_2O:HF at room temperature for 30 s) to remove any native oxide. Next, ozone treatment was performed in situ within the ALD chamber to improve the quality and surface of the chemically -grown SiO_2. Subsequently, Zr:HfO_2 was deposited at 270 °C by ALD; a fixed 4:1 ratio and sequence between the HfO_2 monolayer and the ZrO_2 monolayer set the stoichiometry of the film, in which 10 ALD cycles

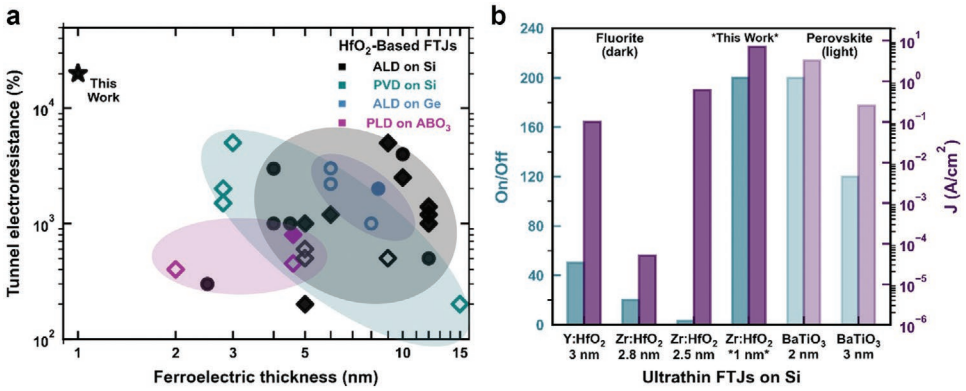

Figure 4. 1 nm Zr:HfO_2 FTJ benchmarked against HfO_2-based FTJ literature and perovskite-based FTJs on Si. a) Comparison of the 1 nm Zr:HfO_2 FTJs in this work (black star) to reported HfO_2-based FTJs as a function of ferroelectric thickness and polarization-driven TER, considering all HfO_2-based deposition techniques on all underlying templates. Open (filled) symbols represent ferroelectric (composite ferroelectric-dielectric) barriers; diamond (circle) symbols represent MIM (MIS) structures. The thickness axis serves as a gauge of the current density J_{ON} (J_{ON} was not available from all references). The 1-nm Zr:HfO_2 FTJ presented in this work demonstrates the largest polarization-driven TER and thinnest ferroelectric barrier reported thus far across all HfO_2-based FTJ literature, desirable for scaled FTJ applications.[50] The following HfO_2-based FTJs references are considered: epitaxial PLD-deposited MFM-structures[20,30] and MFIM-structures,[31] sputtering-deposited MFM structures,[17,39,60,61] ALD-deposited MFM structures,[62–64] MFIM-structures,[18,19,49,65–70] MFS-structures[45,71,72] and MFIS-structures.[43,69,73–77] Reports of non-polarization-driven resistive switching in HfO_2-based FTJs are not considered (Supporting Information). b) Comparison of the 1 nm Zr:HfO_2 FTJs in this work to ultrathin (sub-3 nm) HfO_2-based FTJs and perovskite-based FTJs deposited on Si, considering polarization-driven ON/OFF conductance ratio (J_{ON}/J_{OFF}) and ON current density (J_{ON}). J_{ON} is reported at 250 mV read voltage, except for Y:HfO_2 (3 nm)[39] (500 mV), 2.5 nm Zr:HfO_2 (200 mV)[74] and 2.8 nm[61] Zr:HfO_2 (200 mV). For this work on 1 nm Zr:HfO_2, J_{ON} is consistent across various capacitor areas (Figure S3). The Y:HfO_2 (3 nm)[39] and Zr:HfO_2 (2.8 nm)[61] ferroelectrics are deposited by sputtering (PVD), while the Zr:HfO_2 (2.5 nm)[74] and Zr:HfO_2 (1 nm, this work) ferroelectrics are deposited by the CMOS-compatible ALD technique.[26] The $BaTiO_3$ (2 nm)[53] and $BaTiO_3$ (3 nm)[52] examples are grown by PLD on thick perovskite-buffered Si/SiO_x ($SrTiO_3$ perovskite transition layer, $La_{1-x}Sr_xMnO_3$ bottom electrode).

corresponded to 1 nm of Zr:HfO_2 film, as confirmed by X-ray reflectivity (Figure S1, Supporting Information). The gate metal (W) was deposited by sputtering at room temperature, and final post-metallization annealing was performed at 500 °C (1 min, N_2) to stabilize the desired polar orthorhombic phase. Further details pertaining to ALD growth conditions, post-deposition processing, etc. are outlined in a previous work.[23]

FTJ Fabrication: For capacitor structures (*I–V* characterization), the micron-sized top electrodes of various areas were defined by photolithography and selective etching of the top W metal layer. For bare ferroelectric films (structural studies), the top metal was removed by chemical etching to expose the gate oxide surface. All thin film synthesis was performed at UC Berkeley; processing was performed at the UC Berkeley Marvell Nanofabrication Laboratory.

X-ray Reflectivity: Synchrotron X-ray reflectivity (XRR) of ultrathin Zr:HfO_2 films (Figure S1, Supporting Information)—performed at Sector 33-BM-C beamline of the Advanced Photon Source, Argonne National Laboratory and at Beamline 2-1 of the Stanford Synchrotron Radiation Lightsource, SLAC National Accelerator Laboratory—confirmed the thickness of sub-2 nm films. Fitting analysis was performed with the GenX fitting algorithm.[54] The extracted growth rate—≈ 1 Å/cycle—was consistent with ALD-grown Zr:HfO_2 demonstrated in a previous work.[23]

In-Plane Grazing Incidence Diffraction: Synchrotron in-plane grazing-incidence diffraction (GID) (Figure 1b) was performed at Sector 33-ID-D beamline of the Advanced Photon Source, Argonne National Laboratory. A Pilatus 100K Area Detector collected diffraction flux from the in-plane grazing incidence geometry; the region-of-interest on the Pilatus detector was set to be long in the vertical direction to amplify the relevant diffracted flux. In-plane GID fixed the out-of-plane grazing angle ($\delta = 0.9°$)—such that the sample horizon sits low enough on the Pilatus detector—while the detector was swept in-plane (ν spanned 8–50°); the corrected Bragg angle (2θ) over which the data were plotted and indexed was determined from the relationship $\cos 2\theta = \cos \nu \cdot \cos \delta$ set by the geometry of the experimental setup. The X-ray source was fixed at 16 keV ($\lambda = 0.775$ Å). In-plane geometry allowed for sampling of multiple lattice planes and finer-width reflections to enable clear indexing to the polar orthorhombic ($Pca2_1$) fluorite structure in 1 nm Zr:HfO_2 films (Figure 1b).

2D Diffraction: 2D reciprocal space maps (Figure 1c) were measured at Beamline 11-3 of the Stanford Synchrotron Radiation Lightsource, SLAC National Accelerator Laboratory. Rayonix MX225 CCD area detector collected diffraction flux in gazing incidence (< 0.20°) geometry; the X-ray source (50 microns vertical x 150 microns horizontal beam size) was fixed at 12.7 keV. The sample-detector work distance was set to 80 mm to enable detection of a wide region of reciprocal space (Q-range 0.2 to 5 Å;$^{-1}$) at the expense of real space resolution (d-spacing or θ). The 2D diffraction scans—in which a wide portion of the entire reciprocal space was collected simultaneously, rather than at discrete regions in Q_x–Q_y space—were averaged over data collection time and for repeated scans. These measurement features, in tandem with the high X-ray flux afforded by the synchrotron source, enabled sufficient diffraction signal detection and contrast in films just one nanometer in thickness. Data analysis was performed with Nika, an Igor Pro package for correction, calibration and reduction of 2D area-detector data into 1D data.[55] The 2D reciprocal space slices on bare 1 nm Zr:HfO_2 films displayed regions of concentrated intensity (Figure 1c) rather than isotropic polycrystalline-like rings, consistent with the presence of highly-oriented films.

Piezoresponse Microscopy: Piezoresponse force microscopy (PFM) measurements were performed using a commercial scanning probe microscope (Asylum MFP-3D) at UC Berkeley. Dual-frequency resonance-tracking PFM[56] was conducted using a conductive Pt/Ir-coated probe tip (NanoSensor PPP-EFM) to image written domain structures (Figure 1d) and measure switching-spectroscopy (SS)[57] piezoelectric hysteresis loops (Figure 2c). Resonance-enhanced PFM increases the signal to noise ratio for the detection of out-of-plane electric polarization, critical for ultrathin films. Contact was made to the heavily doped Si substrate for grounding and voltage was applied to the top W electrodes. Switching spectroscopy hysteresis loops were measured on W capacitor structures to help eliminate electrostatic artifacts from the tip,[58] mitigate possible electromechanical contributions,[59] and to yield more confined electric fields. Further scanning probe microscopy demonstrating ferroelectricity in these 1 nm Zr:HfO_2 films is detailed in a previous work.[23]

Conductive Atomic Force Microscopy: CAFM measurements were performed using a commercial scanning probe microscope (Asylum

MFP-3D) with a dual-gain ORCA module, which allowed for the measurement of up to 10 μA of current, at UC Berkeley. CAFM measurements were conducted using conductive Pt-Ir tips from Rocky Mountain Nanotechnologies (25PtIr300B). Once the film was poled with a voltage profile, current maps were obtained by scanning the surface with the tip held at a fixed 800 mV DC bias (significantly below the coercive voltage). To establish polarization-driven resistive switching, current maps were measured after PFM phase maps (Figure 1e). The current maps mimick the phase contrast, indicating the tunneling electroresistance could be attributed to the differing polarization states. To further establish evidence of polarization-dependent resistive switching, the Zr:HfO_2 surface was poled with increasing voltage from −3 V (OFF state) to 3 V (ON state) and subsequently measured with CAFM (Figure 1f) at a fixed DC bias (800 mV).

DC I–V Measurements: Tunnel current measurements were performed using a commercial Semiconductor Device Analyzer (Agilent B1500). Samples were patterned into micron-sized capacitors of various area, with W as the top electrode, and heavily doped Si (10^{19} cm^{-3}) as the bottom contact. 19 micron W tips (DCP-HTR 154-001, FormFactor) made electrical contact within a commercial probe station (Cascade Microtech); voltage was applied to the W top electrodes and the heavily doped Si bottom electrode was grounded. The FTJ devices were set to either the high current or low current state by applying a 500 ms write pulse (+3.0 V for the high current state, −2.7 V for the low current state). To read the FTJ state, linear I–V_{read} sweeps were measured between ±500 mV after programming the FTJ device; ±500 mV is well below the coercive field for 1 nm Zr:HfO_2 on SiO_2-buffered Si. Larger voltages were not used in the linear I–V_{read} sweeps in order to minimize read disturbance.

Pulsed I–V Measurements: Tunnel current measurements were performed an Agilent B1500 with a high voltage semiconductor pulse generator unit (HV-SPGU). Pulsed I–V_{write} hysteresis (Figures 2d and 3d) maps were conducted using the arbitrary linear waveform generator (ALWG) with 100 ms write pulses followed by 100 ms read pulses at 200 mV. In order to reduce the effect of capacitive displacement currents that emerge from voltage changes in the waveform, only the middle 50 ms of the 100 ms read pulse is averaged in order to determine the read current. Endurance cycling measurements (Figure 3e) were conducted with +2.8/−2.5 V 100 ms pulses generated by the HV-SPGU. Slightly lower write voltages were used compared to the linear I–V sweeps in order to increase endurance in exchange for a slight decrease in TER. In order to read out the device after "N" cycles, two 100 ms write pulses were used to definitively set the device into either the high or low current state and was then followed by a linear I–V_{read} sweep between ±300 mV (Figure 3g). Similarly, to characterize the breakdown behavior (Figure S4, Supporting Information), FTJs were cycled as a function of cycling voltage with 100 ms $\pm V_{cycle}$ pulses until dielectric breakdown was observed. For retention measurements (Figure 3f), the FTJ devices were programmed to the high current state (+3.0 V) and low current state (−2.7 V) with a 500 ms write pulse and were subsequently read out at periodic time intervals with a linear I–V sweep between ±300 mV (Figure 3h). Again, ±300 mV is well below the coercive field for 1 nm Zr:HfO_2 on SiO_2-buffered Si.

Supporting Information

Supporting Information is available from the Wiley Online Library or from the author.

Acknowledgements

S.S.C. and N.S. contributed equally to this work. This research was supported in part by the following: the Berkeley Center for Negative Capacitance Transistors (BCNCT); Applications and Systems-Driven Center for Energy-Efficient Integrated NanoTechnologies (ASCENT), one of the six centres in the Joint University Microelectronics Program (JUMP) initiative, a Semiconductor Research Corporation (SRC) program sponsored by Defense Advanced Research Projects Agency (DARPA); the DARPA Foundation Required for Novel Compute (FRANC) programme. This research used resources of the Advanced Photon Source, a U.S. Department of Energy (DOE) Office of Science User Facility operated for the DOE Office of Science by Argonne National Laboratory under Contract No. DE-AC02-06CH11357. Use of the Stanford Synchrotron Radiation Light source, SLAC National Accelerator Laboratory, was supported by the U.S. Department of Energy, Office of Science, Office of Basic Energy Sciences under Contract No. DE-AC02-76SF00515.

Conflict of Interest

The authors declare no conflict of interest.

Data Availability Statement

The data that support the findings of this study are available from the corresponding author upon reasonable request.

[1] T. Mikolajick, U. Schroeder, S. Slesazeck, *IEEE Trans. Electron Devices* **2020**, *67*, 1434.
[2] A. I. Khan, A. Keshavarzi, S. Datta, *Nature Electron.* **2020**, *3*, 588.
[3] M. E. Lines, A. M. Glass, *Principles and Applications of Ferroelectrics and Related Materials*, Oxford University Press **1977**.
[4] M. Dawber, K. M. Rabe, J. F. Scott, *Rev. Mod. Phys.* **2005**, *77*, 1083.
[5] D. G. Schlom, S. Guha, S. Datta, *MRS Bull.* **2008**, *33*, 1017.
[6] T. S. Böscke, J. Müller, D. Bräuhaus, U. Schröder, U. Böttger, *Appl. Phys. Lett.* **2011**, *99*, 102903.
[7] M. H. Park, Y. H. Lee, T. Mikolajick, U. Schroeder, C. S. Hwang, *MRS Commun.* **2018**, *8*, 795.
[8] M. H. Park, Y. H. Lee, H. J. Kim, Y. J. Kim, T. Moon, K. D. Kim, J. Müller, A. Kersch, U. Schroeder, T. Mikolajick, C. S. Hwang, *Adv. Mater.* **2015**, *27*, 1811.
[9] J. Y. Park, K. Yang, D. H. Lee, S. H. Kim, Y. Lee, P. R. S. Reddy, J. L. Jones, M. H. Park, *J. Appl. Phys.* **2020**, *128*, 240904.
[10] T. Mikolajick, S. Slesazeck, M. Park, U. Schroeder, *MRS Bull.* **2018**, *43*, 340.
[11] D. Ielmini, H.-S. P. Wong, *Nature Electron.* **2018**, *1*, 333.
[12] Z. Wang, H. Wu, G. W. Burr, C. S. Hwang, K. L. Wang, Q. Xia, J. J. Yang, *Nature Rev. Mater.* **2020**, *5*, 173.
[13] S. Slesazeck, T. Mikolajick, *Nanotechnology* **2019**, *30*, 352003.
[14] E. Y. Tsymbal, H. Kohlstedt, *Science* **2006**, *313*, 181.
[15] V. Garcia, M. Bibes, *Nature Commun.* **2014**, *5*, 4289.
[16] Z. Wen, D. Wu, *Adv. Mater.* **2019**, *32*, 1904123.
[17] Z. Fan, J. Xiao, J. Wang, L. Zhang, J. Deng, Z. Liu, Z. Dong, J. Wang, J. Chen, *Appl. Phys. Lett.* **2016**, *108*, 232905.
[18] S. Fujii, Y. Kamimuta, T. Ino, Y. Nakasaki, R. Takaishi, M. Saitoh, in *2016 IEEE Symp. on VLSI Technology*, IEEE, Piscataway, NJ **2016**, p. 1.

[19] B. Max, M. Hoffmann, S. Slesazeck, T. Mikolajick, in *2018 48th European Solid-State Device Research Conf. (ESSDERC)*, IEEE, Piscataway, NJ **2018**, p. 142.

[20] Y. Wei, S. Matzen, T. Maroutian, G. Agnus, M. Salverda, P. Nukala, Q. Chen, J. Ye, P. Lecoeur, B. Noheda, *Phys. Rev. Appl.* **2019**, *12*, 031001.

[21] H.-J. Lee, M. Lee, K. Lee, J. Jo, H. Yang, Y. Kim, S. C. Chae, U. Waghmare, J. H. Lee, *Science* **2020**, *369*, 1343.

[22] B. Noheda, J. Iniguez, *Science* **2020**, *369*, 1300.

[23] S. S. Cheema, D. Kwon, N. Shanker, R. dos Reis, S.-L. Hsu, J. Xiao, H. Zhang, R. Wagner, A. Datar, M. R. McCarter, C. R. Serrao, A. K. Yadav, G. Karbasian, C.-H. Hsu, A. J. Tan, L.-C. Wang, V. Thakare, X. Zhang, A. Mehta, E. Karapetrova, R. V. Chopdekar, P. Shafer, E. Arenholz, C. Hu, R. Proksch, R. Ramesh, J. Ciston, S. Salahuddin, *Nature* **2020**, *580*, 478.

[24] Y. Wei, P. Nukala, M. Salverda, S. Matzen, H. J. Zhao, J. Momand, A. S. Everhardt, G. Agnus, G. R. Blake, P. Lecoeur, B. J. Kooi, J. Íñiguez, B. Dkhil, B. Noheda, *Nature Mater.* **2018**, *17*, 1095.

[25] C. Ahn, K. Rabe, J. Triscone, *Science* **2004**, *303*, 488.

[26] R. W. Johnson, A. Hultqvist, S. F. Bent, *Mater. Today* **2014**, *17*, 236.

[27] V. Garcia, S. Fusil, K. Bouzehouane, S. Enouz-Vedrenne, N. D. Mathur, A. Barthélémy, M. Bibes, *Nature* **2009**, *460*, 81.

[28] Z. Wen, C. Li, D. Wu, A. Li, N. Ming, *Nature Mater.* **2013**, *12*, 617.

[29] A. Chanthbouala, A. Crassous, V. Garcia, K. Bouzehouane, S. Fusil, X. Moya, J. Allibe, B. Dlubak, J. Grollier, S. Xavier, C. Deranlot, A. Moshar, R. Proksch, N. D. Mathur, M. Bibes, A. Barthélémy, *Nature Nanotechnol.* **2012**, *7*, 101.

[30] M. C. Sulzbach, S. Estandía, X. Long, J. Lyu, N. Dix, J. Gàzquez, M. F. Chisholm, F. Sánchez, I. Fina, J. Fontcuberta, *Adv. Electronic Mater.* **2020**, *6*, 1900852.

[31] M. C. Sulzbach, S. Estandía, J. Gàzquez, F. Sánchez, I. Fina, J. Fontcuberta, *Adv. Funct. Mater.* **2020**, *30*, 2002638.

[32] B. Max, M. Pešić, S. Slesazeck, T. Mikolajick, *J. Appl. Phys.* **2018**, *123*, 134102.

[33] M. Materano, P. D. Lomenzo, A. Kersch, M. H. Park, T. Mikolajick, U. Schroeder, *Inorganic Chem. Front.* **2021**, *8*, 2650.

[34] P. Nukala, M. Ahmadi, Y. Wei, S. de Graaf, E. Stylianidis, T. Chakrabortty, S. Matzen, H. W. Zandbergen, A. Björling, D. Mannix, D. Carbone, B. Kooi, B. Noheda, *Science* **2021**, *372*, 630.

[35] M. D. Glinchuk, A. N. Morozovska, A. Lukowiak, W. Stręk, M. V. Silibin, D. V. Karpinsky, Y. Kim, S. V. Kalinin, *J. Alloys Compounds* **2020**, *830*, 153628.

[36] *J. Mater. Chem. A* **2020**, *8*, 14023.

[37] V. Rouco, R. E. Hage, A. Sander, J. Grandal, K. Seurre, X. Palermo, J. Briatico, S. Collin, J. Trastoy, K. Bouzehouane, A. I. Buzdin, G. Singh, N. Bergeal, C. Feuillet-Palma, J. Lesueur, C. Leon, M. Varela, J. Santamaría, J. E. Villegas, *Nature Commun.* **2020**, *11*, 658.

[38] S. S. Fields, S. W. Smith, P. J. Ryan, S. T. Jaszewski, I. A. Brummel, A. Salanova, G. Esteves, S. L. Wolfley, M. D. Henry, P. S. Davids, J. F. Ihlefeld, *ACS Appl. Mater. Interfaces* **2020**, *12*, 26577.

[39] X. Tian, A. Toriumi, in *2017 IEEE Electron Devices Technology and Manufacturing Conf. (EDTM)*, IEEE, Piscataway, NJ **2017**, p. 63.

[40] Y. Wei, S. Matzen, C. P. Quinteros, T. Maroutian, G. Agnus, P. Lecoeur, B. Noheda, *npj Quantum Mater.* **2019**, *4*, 62.

[41] S. Starschich, S. Menzel, U. Böttger, *Appl. Phys. Lett.* **2016**, *108*, 032903.

[42] M. Pešić, F. P. G. Fengler, L. Larcher, A. Padovani, T. Schenk, E. D. Grimley, X. Sang, J. M. LeBeau, S. Slesazeck, U. Schroeder, T. Mikolajick, *Adv. Funct. Mater.* **2016**, *26*, 4601.

[43] V. Mikheev, A. Chouprik, Y. Lebedinskii, S. Zarubin, A. M. Markeev, A. V. Zenkevich, D. Negrov, *Nanotechnology* **2020**, *31*, 215205.

[44] S. Li, D. Zhou, Z. Shi, M. Hoffmann, T. Mikolajick, U. Schroeder, *Adv. Electronic Mater.* **2020**, *6*, 2000264.

[45] Y. Goh, S. Jeon, *Nanotechnology* **2018**, *29*, 335201.

[46] F. Mo, Y. Tagawa, T. Saraya, T. Hiramoto, M. Kobayashi, in *2018 IEEE Int. Electron Devices Meeting (IEDM)*, IEEE, Piscataway, NJ **2018**, p. 16.3.1.

[47] M. Y. Zhuravlev, Y. Wang, S. Maekawa, E. Y. Tsymbal, *Appl. Phys. Lett.* **2009**, *95*, 052902.

[48] H.-H. Huang, T.-Y. Wu, Y.-H. Chu, M.-H. Wu, C.-H. Hsu, H.-Y. Lee, S.-S. Sheu, W.-C. Lo, T.-H. Hou, in *2019 IEEE Int. Electron Devices Meeting (IEDM)*, IEEE, Piscataway, NJ **2019**, p. 32.2.1.

[49] B. Max, M. Hoffmann, S. Slesazeck, T. Mikolajick, *IEEE J. Electron Devices Soc.* **2019**, *7*, 1175.

[50] S. Fujii, M. Saitoh, In *Ferroelectricity in Doped Hafnium Oxide: Materials, Properties and Devices*, Elsevier, **2019**, 437.

[51] M. Y. Zhuravlev, R. F. Sabirianov, S. S. Jaswal, E. Y. Tsymbal, *Phys. Rev. Lett.* **2005**, *94*, 246802.

[52] Z. Li, X. Guo, H.-B. Lu, Z. Zhang, D. Song, S. Cheng, M. Bosman, J. Zhu, Z. Dong, W. Zhu, *Adv. Mater.* **2014**, *26*, 7185.

[53] R. Guo, Z. Wang, S. Zeng, K. Han, L. Huang, D. G. Schlom, T. Venkatesan, Ariando, J. Chen, *Sci. Rep.* **2015**, *5*, 12576.

[54] M. Björck, G. Andersson, *J. Appl. Crystallogr.* **2007**, *40*, 1174.

[55] J. Ilavsky, *J. Appl. Crystallogr.* **2012**, *45*, 324.

[56] B. J. Rodriguez, C. Callahan, S. V. Kalinin, R. Proksch, *Nanotechnology* **2007**, *18*, 475504.

[57] S. Jesse, H. N. Lee, S. V. Kalinin, *Rev. Sci. Instruments* **2006**, *77*, 073702.

[58] S. Hong, J. Woo, H. Shin, J. Jeon, E. Y. Pak, E. L. Colla, N. Setter, E. Kim, K. No, *J. Appl. Phys.* **2001**, *89*, 1377.

[59] R. K. Vasudevan, N. Balke, P. Maksymovych, S. Jesse, S. V. Kalinin, *Appl. Phys. Rev.* **2017**, *4*, 021302.

[60] F. Ambriz-Vargas, G. Kolhatkar, R. Thomas, R. Nouar, A. Sarkissian, C. Gomez-Yáñez, M. A. Gauthier, A. Ruediger, *Appl. Phys. Lett.* **2017**, *110*, 093106.

[61] F. Ambriz-Vargas, G. Kolhatkar, M. Broyer, A. Hadj-Youssef, R. Nouar, A. Sarkissian, R. Thomas, C. Gomez-Yáñez, M. A. Gauthier, A. Ruediger, *ACS Appl. Mater. Interfaces* **2017**, *9*, 13262.

[62] L. Chen, T.-Y. Wang, Y.-W. Dai, M.-Y. Cha, H. Zhu, Q.-Q. Sun, S.-J. Ding, P. Zhou, L. Chua, D. W. Zhang, *Nanoscale* **2018**, *10*, 15826.

[63] Y. Goh, J. Hwang, S. Jeon, *ACS Appl. Mater. Interfaces* **2020**, *12*, 57539.

[64] J. Yoon, S. Hong, Y. W. Song, J.-H. Ahn, S.-E. Ahn, *Appl. Phys. Lett.* **2019**, *115*, 153502.

[65] B. Max, T. Mikolajick, M. Hoffmann, S. Slesazeck, T. Mikolajick, in *2019 IEEE 11th Int. Memory Workshop (IMW)*, IEEE, Piscataway, NJ **2019**, p. 1.

[66] R. Berdan, T. Marukame, S. Kabuyanagi, K. Ota, M. Saitoh, S. Fujii, J. Deguchi, Y. Nishi, in *2019 Symp. on VLSI Technology*, IEEE, Piscataway, NJ **2019**, p. T22.

[67] K. Ota, J. Deguchi, S. Fujii, M. Saitoh, M. Yamaguchi, R. Berdan, T. Marukame, Y. Nishi, K. Matsuo, K. Takahashi, Y. Kamiya, S. Miyano, in *2019 IEEE Int. Electron Devices Meeting (IEDM)*, IEEE, Piscataway, NJ **2019**, p. 6.2.1.

[68] J. Hwang, Y. Goh, S. Jeon, *IEEE Trans. Electron Devices* **2021**, *68*, 841.

[69] Y.-S. Kuo, S.-Y. Lee, C.-C. Lee, S.-W. Li, T.-S. Chao, *IEEE Trans. Electron Devices* **2021**, *68*, 879.

[70] T.-Y. Wu, T.-S. Chang, H.-Y. Lee, S.-S. Sheu, W.-C. Lo, T.-H. Hou, H.-H. Huang, Y.-H. Chu, C.-C. Chang, M.-H. Wu, C.-H. Hsu, C.-T. Wu, M.-C. Wu, W.-W. Wu, in *2019 IEEE Int. Electron Devices Meeting (IEDM)*, IEEE, Piscataway, NJ **2019**, p. 6.3.1.

[71] Y. Goh, S. Jeon, *Appl. Phys. Lett.* **2018**, *113*, 052905.

[72] J. Hwang, Y. Goh, S. Jeon, *IEEE Electron Device Lett.* **2020**, *41*, 1193.
[73] M. Kobayashi, Y. Tagawa, F. Mo, T. Saraya, T. Hiramoto, *IEEE J. Electron Devices Soc.* **2019**, *7*, 134.
[74] A. Chouprik, A. Chernikova, A. Markeev, V. Mikheev, D. Negrov, M. Spiridonov, S. Zarubin, A. Zenkevich, *Microelectronic Eng.* **2017**, *178*, 250.
[75] V. Mikheev, A. Chouprik, Y. Lebedinskii, S. Zarubin, Y. Matveyev, E. Kondratyuk, M. G. Kozodaev, A. M. Markeev, A. Zenkevich, D. Negrov, *ACS Appl. Mater. Interfaces* **2019**, *11*, 32108.
[76] H. Ryu, H. Wu, F. Rao, W. Zhu, *Sc. Rep.* **2019**, *9*, 20383.
[77] A. Shekhawat, G. Walters, N. Yang, J. Guo, T. Nishida, S. Moghaddam, *Nanotechnology* **2020**, *31*, 39LT01.